

EvolVED: Evolutionary Embeddings to Understand the Generation Process of Diffusion Models

Vidya Prasad, Hans van Gorp, Christina Humer, Ruud J. G. van Sloun, Anna Vilanova, and Nicola Pezzotti

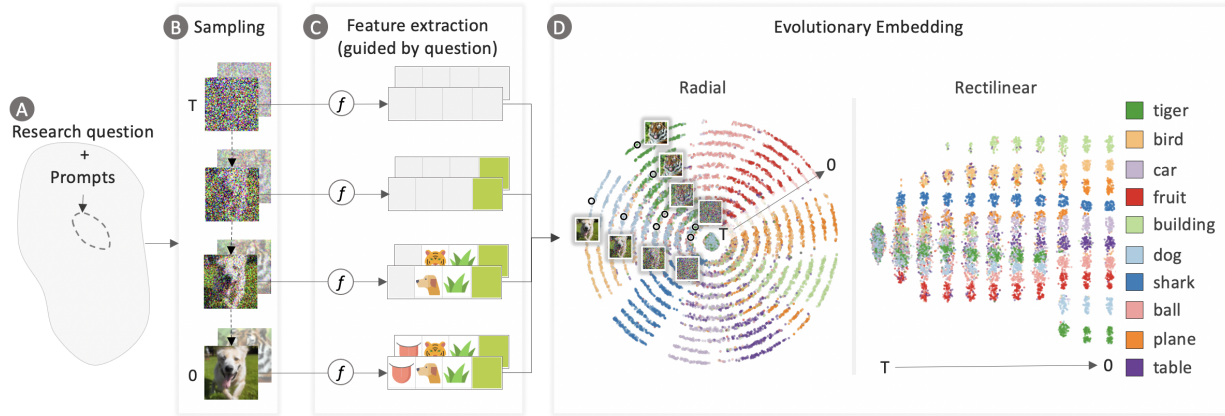


Fig. 1: Understanding the evolutionary generation process in diffusion models with *EvolVED*. (A) Predefined research questions with tailored prompts. (B) Example of sampling the generative space of GLIDE [26]. (C) Semantic object and context features of noisy images (\mathbf{h}_{t-1}^i) extracted at every 10^{th} step using an ImageNet classifier [2], capturing key features aligned with the research objectives. (D) The evolutionary embedding method explicitly encodes iterations. The inner ring in the radial layout and the leftmost line in the rectilinear layout represent the initial generation steps, progressing outward or towards the right to the final steps. Clusters such as “dogs” are initially confused with “tigers” due to their presence on grass but gradually become distinct towards the later steps.

Abstract— Diffusion models, widely used in image generation, rely on iterative refinement to generate images from noise. Understanding this data evolution is important for model development and interpretability, yet challenging due to its high-dimensional, iterative nature. Prior works often focus on static or instance-level analyses, missing the iterative and holistic aspects of the generative path. While dimensionality reduction can visualize image evolution for few instances, it does not preserve the iterative structure. To address these gaps, we introduce *EvolVED*, a method that presents a holistic view of the iterative generative process in diffusion models. *EvolVED* goes beyond instance exploration by leveraging predefined research questions to streamline generative space exploration. Tailored prompts aligned with these questions are used to extract intermediate images, preserving iterative context. Relevant feature extractors are used to trace the evolution of key image features, addressing the complexity of high-dimensional outputs. Central to *EvolVED* is a novel evolutionary embedding algorithm that encodes iterative steps while maintaining semantic relations. It enhances the visualization of data evolution by clustering semantically similar elements within each iteration with t-SNE, grouping elements by iteration, and aligning an instance’s elements across iterations. We present rectilinear and radial layouts to represent iterations and support exploration. We apply *EvolVED* to diffusion models like GLIDE and Stable Diffusion, demonstrating its ability to provide valuable insights into the generative process.

Index Terms—Explainable AI, diffusion models, dimensionality reduction, evolutionary embedding, high dimensional, visual analytics

1 INTRODUCTION

Diffusion models have gained popularity across various applications [53], like generation, inverse problems, segmentation, and anomaly detection. They effectively generate diverse and high-quality samples by progressively corrupting data with noise, followed by an iterative reconstruction. At each step, a trainable DL model (such as U-Net [42]) processes an intermediate noisy image, the iteration number, and optionally a prompt, generating a less noisy image. This evolution goes from an initial state of pure noise to a coherent image (see Fig. 2).

Analyzing data evolution offers insights beyond image changes, revealing model learnings, data distribution evolution [29], and the decision-making dynamics of dataset modes. Such knowledge is valu-

able for refining models and training [7, 15, 23, 54], controlling generation [9, 29, 52], improving performance [38, 43], and identifying feature entanglements [54]. Despite these needs, there is limited support for holistic analysis of the evolutionary process.

Current explainable AI methods mainly analyze classification models [37], which have final-layer 1D representations and single-step outputs. In contrast, diffusion models involve iterative evolution and high-dimensional outputs, limiting the value of static analysis methods. Additionally, these image-to-image translation models internally lack a single low-dimensional latent representation, complicating the identification of a meaningful feature space for analysis [37]. While methods to analyze diffusion models exist, they are limited in their ability to go beyond analyzing the iterative generative process of a single instance. They often focus on high-level insights, such as feature granularity [29, 38], or explore randomly selected instances [28], insufficient for a comprehensive understanding. Some methods use synthetic low-dimensional datasets [15] and local latent structure analyses [29] to illustrate this process but they offer limited insights into the feature evolution on real data sets. Dimensionality reduction (DR) tech-

- V. Prasad, H. van Gorp, R. J. G. van Sloun, A. Vilanova, and N. Pezzotti are with Eindhoven University of Technology. E-mail: v.prasad@tue.nl
- C. Humer is with Johannes Kepler Universität Linz.
- H. van Gorp and N. Pezzotti are with Philips.

THIS IS A PREPRINT.

niques [22, 49] commonly used to visualize high-dimensional spaces, can be directly used to show feature evolution over a few instances [18]. However, they are not designed to support the analysis of the evolutionary aspect of diffusion data. The stochastic cluster placing in DR methods such as t-SNE [49] or UMAP [22], further complicates tracing data evolution and hinders analysis. There is a need for a method that preserves the iterative structure while providing a holistic view of data evolution to effectively understand and develop diffusion models, as existing methods fail to address both aspects together.

To address these gaps, we present *EvolvED*, a method designed to provide a holistic understanding of data evolution within the generative process of diffusion models (see Fig. 1). Unlike prior works, *EvolvED* enables a targeted approach relying on user-defined research questions. This facilitates a focused investigation into specific characteristics, such as the progression of natural objects or artistic styles. While the broader aim is to analyze the entire generative space, *EvolvED* narrows its focus to manage the complexity of the space. We sample the diffusion model using prompts tailored to the research question. We extract intermediate images at multiple stages of the generative process to capture the stepwise progression of the model output. Since diffusion models internally lack a unified low-dimensional latent space per step, we use external feature extractors to isolate and track attributes of interest aligned with the research question from interim images. Finally, we propose a novel *evolutionary embedding* algorithm that enhances t-SNE to be able to capture the evolving structure of generative processes. *Evolutionary* refers to the method’s ability to consider the dynamic aspects of the generated data, allowing to trace changes through the iterations. Our algorithm augments the t-SNE cost function to contain three key components: 1) clustering semantically similar elements, 2) grouping elements of the same iteration, and 3) aligning the same instance across iterations. We introduce rectilinear and radial layouts to explicitly represent the iterations. We demonstrate *EvolvED*’s utility and versatility with two prominent diffusion models, GLIDE [26] and StableDiffusion [41], across different research questions. By exploring how data and their specific attributes evolve, we gain valuable insights into the generation process of diffusion models. Our contributions are:

- *EvolvED*, a method to holistically understand data evolution within diffusion models. It includes a pipeline to sample the generative space, extract relevant features, and visualize their evolution during generation¹.
- A novel *evolutionary embedding* algorithm that visualizes the evolutionary nature of diffusion models.
- *EvolvED*’s applicability is evaluated via three cases with diverse research questions and models.

2 BACKGROUND

Diffusion models [13, 25, 44] aim to approximate the true distribution $u(\mathbf{h}_0)$ of training data \mathbf{h}_0 . For this, training data is gradually corrupted with Gaussian noise, resulting in a sequence of data sets $\mathbf{h}_1, \dots, \mathbf{h}_t, \dots, \mathbf{h}_T$ that define different spaces. The amount of noise added varies across iterations t , and is defined by a scheduler. This corruption process of moving from the original data distribution $u(\mathbf{h}_0)$ to noise $u(\mathbf{h}_T)$, is called the forward process (see Fig. 2).

For generation, a single model v_θ (often a U-Net [42]) is trained to estimate the noise needed to go from a noisy image instance i at any iteration t , \mathbf{h}_t^i , to the final denoised image \mathbf{h}_0^i . We refer to this *step-wise denoised estimate* of instance i at iteration t as $\mathbf{h}_{t_0}^i$. A known noise level based on the scheduler is added back to $\mathbf{h}_{t_0}^i$ to generate the *step-wise noisy estimate* \mathbf{h}_{t-1}^i . The iterative process of estimating \mathbf{h}_{t-1}^i from \mathbf{h}_t^i continues until $t = 0$ and is called the reverse generative process (see Fig. 2). Further details can be found in the original papers [13, 25]. For our analysis, we extract the noisy image \mathbf{h}_t^i and denoised estimate $\mathbf{h}_{t_0}^i$ of the final denoised image at each iteration t across instances i .

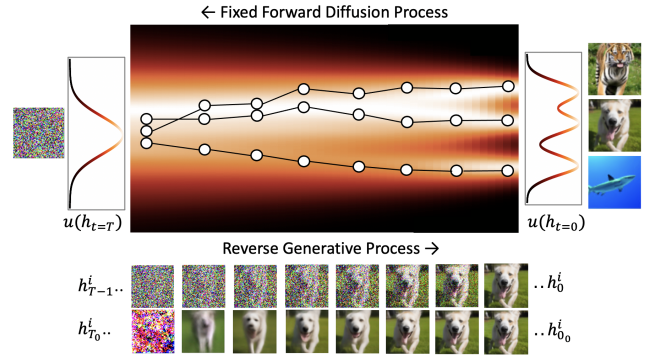


Fig. 2: Theoretical representation of the diffusion process [45], where the training data distribution $u(\mathbf{h}_0)$ is represented as a 1D Gaussian. During generation (left to right), instances evolve from noise \mathbf{h}_T to a coherent image \mathbf{h}_0 . Intermediate steps also produce fuzzy, denoised estimates $\mathbf{h}_{t_0}^i$, which gradually refine into clearer images on convergence.

t-Distributed Stochastic Neighbourhood Embedding or t-SNE [49] is a non-linear DR method widely used for visualizing high-dimensional data. It aims to preserve the neighborhoods between the high-dimensional data points in a low-dimensional output space. For this, t-SNE translates distances between the high-dimensional points as a symmetric joint probability distribution P . Similarly, a joint probability distribution Q describes the low-dimensional similarity. The goal is to achieve a mapping or an embedding in the low-dimensional space Q that faithfully represents P . This is achieved by optimizing the positions of the low-dimensional points via a cost C , which is the KL divergence between P and Q ,

$$C = KL(P||Q) = \sum_i^n \sum_{j \neq i}^n p^{ij} \ln \frac{p^{ij}}{q^{ij}} \quad (1)$$

p^{ij} is the similarity between two high-dimensional points \mathbf{h}^i and \mathbf{h}^j of a data set \mathbf{h} . It is based on their conditional probabilities p^{ij} and p^{ji} , shown in Eq. (2). p^{ji} is the likelihood that \mathbf{h}^j is selected as the neighbor of \mathbf{h}^i based on a Gaussian probability density function centered at \mathbf{h}^i with variance σ_i . σ_i is defined based on the local density of \mathbf{h}^i in the high-dimensional space and a defined perplexity parameter.

$$p^{ij} = \frac{p^{ij} + p^{ji}}{2N}, \text{ where, } p^{ji} = \frac{\exp(-\|\mathbf{h}^i - \mathbf{h}^j\|^2 / (2\sigma_i^2))}{\sum_{k \neq i} \exp(-\|\mathbf{h}^i - \mathbf{h}^k\|^2 / (2\sigma_i^2))} \quad (2)$$

For the low-dimensional space Q , whose point positions need to be optimized, a student t-distribution with one degree of freedom is used to compute the joint probability distribution. The similarity q^{ij} between two low-dimensional points \mathbf{l}^i and \mathbf{l}^j is then given by,

$$q^{ij} = \frac{(1 + \|\mathbf{l}^i - \mathbf{l}^j\|^2)^{-1}}{\sum_{k \neq m} (1 + \|\mathbf{l}^k - \mathbf{l}^m\|^2)^{-1}} \quad (3)$$

Our paper employs the vanilla t-SNE [49] to identify the similarity between high-dimensional images \mathbf{h}_t^i from the diffusion model. We augment t-SNEs’ KL divergence cost function by introducing components to group images within an iteration t and align images of an instance i across iterations.

3 RELATED WORK

Interpreting Diffusion Models: While exploring and understanding the inner workings of diffusion models is important for leveraging their full potential and inspiring further research [5], their inherent complexity of high-dimensional evolutionary processes poses challenges [18, 50], even for domain experts.

Literature has shown the purpose of each iterative step, which correlates with the varying granularity of visual concepts [7, 28, 38, 43]. Prior

¹The code is available at <https://github.com/vidyaprds/EvolvED>

works have examined the local latent structure around an instance in the diffusion process [17, 29] with methods like Riemannian geometry [29]. While the goal was image editing, they also shed light on the granularity of features across steps [29]. However, it is crucial to understand the evolution of actual features to understand the root failure causes and enable downstream development [20, 28]. Most of these works focus on applying insights to improved models rather than generic means of visualizing the evolutionary process to support understanding.

Pixel-level attribution maps explain relations between generated image areas and prompt keywords via cross-attention keyword–pixel scores in the denoising network of diffusion models [46]. These maps have been used for controlling output images [6, 11, 30, 47]. Saliency map methods were extended to diffusion models to study the model’s focus in each iteration and how it evolves [28]. However, these existing approaches primarily concentrate on individual samples, creating a gap in understanding the global evolutionary process, which is our focus.

While visual analytics (VA) has provided a more generic means to analyze and understand complex DL models, most works focus, for example, on classification tasks [34, 37, 51], or generative adversarial networks [14], which do not contain the iterative complexities of diffusion models. Methods to understand text-to-image data distributions have been proposed [55], but they primarily focus on analyzing final outputs rather than the full evolutionary process. Lee et al. [18] proposed DiffusionExplainer to provide insights into the full generative process of a diffusion model at an instance level. It projected intermediate noisy images via UMAP to a 2D space, offering insights into how individual instances evolve. However, our goal is to extend this to a holistic understanding of the entire evolutionary process. Visualizing the full evolutionary process offers deeper insights into how features emerge. This could help inform model design, for example, by revealing how schedulers impact generation informing model distillation [23] or identifying where feature entanglements occur, enabling more targeted adjustments [54].

Visualizing high-dimensional evolutionary data: DR techniques, like t-SNE or UMAP, offer value in visualizing data evolution over a few instances [18]. Such methods have also been used in visualizing data evolution globally in strategic games [12]. However, they do not preserve the iterative structure inherent in diffusion models due to their stochastic nature, which is amplified when visualizing large-scale samples. Neural network features across layers [40] or optimization iterations [19] have been visualized with one embedding per layer, making it challenging to study evolution. While parallel coordinates are a popular means to visualize evolutionary data in other applications [3, 10], projecting high-dimensional data onto a single dimension presents challenges. Luo et al. [21] incorporate soft Gaussian constraints to position points within an iteration close together. Methods using vertical distances between pairs of connected points can help with alignment of these points [4, 32]. However, they overlook that early iterations in diffusion models contain less information than later ones, making equal visual space allocation inefficient for our case. Our evolutionary embedding addresses this by combining soft iteration displacement and instance alignment constraints and optimizes space usage across steps to better study diffusion model evolution.

4 EVOLVED

The theoretical representation of data evolution in diffusion models [45, 48] in Fig. 2 shows how the data distribution $u(\mathbf{h}_t)$ transitions from a 1D uni-modal Gaussian mode, representing pure noise, to a multi-modal distribution. Such a representation supports understanding the feature space evolution across iterations. However, translating this illustrative example to real high-dimensional, iterative generation spaces produced by real diffusion models is highly complex. To address these challenges, we introduce *EvolvED* (see Fig. 1), a method that employs a structured pipeline to provide a holistic understanding of the iterative and high-dimensional generation process in diffusion models. It begins by utilizing user-defined research questions to narrow the exploration of the vast generative space (see Fig. 1a). *EvolvED*

allows for a targeted investigation into specific image attributes via tailored prompts aligned with the research question. Intermediate images are systematically extracted at multiple stages to capture the iterative progress and data evolution (see Fig. 1b). Given that diffusion models often lack a unified low-dimensional latent representation [37], we propose employing feature extractors to isolate and track the attributes of interest throughout the generative process as shown in Fig. 1c. Finally, to enhance the visualization of this iterative process, we introduce an evolutionary embedding algorithm in Fig. 1d. This algorithm explicitly encodes iterations to enable the visualization of data evolution. Each of these components of *EvolvED* is described below.

4.1 User-Defined Focus & Prompts

The *EvolvED* pipeline starts by defining specific research questions to guide the exploration of the generative space (see Fig. 1a), such as, the “progression of natural objects” to understand which attributes arise when. With these research questions, *EvolvED* aims to navigate the vast generative space. Tailored prompts aligned with these questions must then be defined to ensure a focused analysis of relevant attributes. For example, prompts like “a dog”, “a dog on grass”, or “a dog in water” can help analyze the “progression of natural objects”.

4.2 Sampling Intermediate Data

To capture the model’s iterative nature, we sample the generative space using tailored prompts, extracting intermediate outputs for an instance i across multiple iterations t (see Fig. 1b), rather than just the final output. This data includes the step-wise noisy \mathbf{h}_{t-1}^i and step-wise denoised estimates \mathbf{h}_t^i . The denoised images represent the model’s prediction power of the final image at t , commonly transitioning from fuzzy object shadows to more detailed images (see Fig. 2). \mathbf{h}_t^i is either explicitly predicted or can be implicitly extracted from diffusion models.

4.3 Feature Extraction

Unlike classification models, which have well-defined latent layers for analysis, diffusion models use image-to-image architectures like U-Nets, which lack a unified low-dimensional latent space [37]. The role of each layer shifts across iterations [37, 38], complicating the analysis of high-dimensional intermediate samples. Latent space diffusion models [41] use structured, high-dimensional spatial latent representations, with similar challenges to raw image analysis. Hence, *EvolvED* employs feature extractors f specifically designed to isolate or encode features of interest from high-dimensional images to a lower-dimensional space. These extractors process the intermediate outputs, where $\hat{\mathbf{h}}_{t-1}^i = f(\mathbf{h}_{t-1}^i)$ and $\hat{\mathbf{h}}_t^i = f(\mathbf{h}_t^i)$ represent the extracted features from the step-wise noisy and denoised estimates, respectively. For example, a robust ImageNet classifier f encoding specific attributes like *grass* and *dog* would be effective in analyzing “progression of natural objects”. The feature extractor chosen depends on the research question, as explored in our case studies. While this selection is case-dependent and not the primary focus of our work, we provide guidelines for choosing effective extractors in different scenarios.

- **Correlation of Features and Insights:** Chosen feature extractors must either explicitly (classifiers [2]) or implicitly (encoders [39]) extract features that align with the research question.
- **Reliability on Corrupted Images:** The feature extraction process must remain reliable even in the presence of corruption, such as fuzziness in intermediate images. We evaluate different extractors on both noisy \mathbf{h}_t^i and denoised \mathbf{h}_t^i images to ensure that the features remain meaningful from the early stages of generation.
- **Smooth Transitions:** Ideally, the extracted features should correspond to relevant changes in the images. If the images evolve gradually across iterations, the features should reflect this, and conversely, if the changes are abrupt, the features should capture that as well. This ensures a coherent representation of the instance’s development throughout the diffusion process.

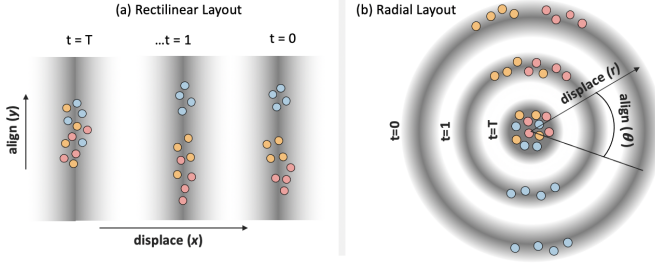


Fig. 3: Evolutionary embedding process for the (a) rectilinear and (b) radial layout. Elements of iterations t are attracted to dark, low-cost areas based on a Gaussian at a displacement value (\bar{x}_t or \bar{r}_t) per t . Elements of an instance across iterations are aligned based on their y or θ .

4.4 Visualization: Evolutionary Embedding

From the previous steps, we obtain one or multiple high-dimensional feature spaces per iteration. Existing DR methods to study high-dimensional data like t-SNE are not designed to preserve the evolutionary context while preserving semantic relations. Hence, we introduce a novel evolutionary embedding algorithm to address these challenges, which is the core *EvoVED*. We consider common layout design choices, i.e., rectilinear and radial layouts [27], to explicitly represent iterations. It allows the visualization of feature evolution while maintaining iterative context (see Fig. 1d). Our evolutionary embedding method projects the extracted features ($\hat{\mathbf{h}}_{t-1}^i$ or $\hat{\mathbf{h}}_{t_0}^i$) to a 2D space. The loss function is defined by three main components:

- **Semantic loss (G1):** Semantically similar elements in the high-dimensional feature space need to be placed together in the low-dimensional projection. This is achieved through the standard t-SNE KL divergence loss [49] per iteration, which preserves the neighborhood structure of the high-dimensional data in the low-dimensional space. It is assumed that the feature space obtained by the previous modules is semantically meaningful.
- **Displacement loss (G2):** Elements belonging to the same iteration must be placed together to study and compare how different data modes evolve. For example the topmost *shark* mode in Fig. 2 emerges sooner than the other objects. Hence, we impose a specific region per iteration of diffusion models using a displacement loss. This loss uses a Gaussian centered around the corresponding iteration offset in the low-dimensional space (see Fig. 1d).
- **Alignment loss (G3):** There should be alignment of components of the same sample i across iterations t to preserve coherence and minimize misalignments in the projections across t due to the stochasticity of t-SNE. Hence, we use an alignment loss that measures the offset in vertical position [4] or angular distance among consecutive pairs of elements of an instance across iterations.

To implement these goals, we define the total loss C as a weighted combination of the three components,

$$C = \alpha * C_s + \beta * C_d + \gamma * C_a \quad (4)$$

C_s , C_d , C_a are the semantic (G1), displacement (G2), and alignment loss (G3) respectively. The combined cost C is minimized via gradient descent with a similar optimization method proposed by van der Maaten [49]. The displacement and alignment losses are additional constraints on each low-dimensional embedding. The semantic t-SNE loss (G1) and displacement loss (G2) are local, i.e., they are applied within an iteration, while the alignment loss (G3) operates across steps by requirement. Since we want to preserve semantic clusters while maintaining the alignment and displacement conditions, the three losses must be modeled as a joint optimization problem with Eq. (4).

Common t-SNE loss (G1): For both layouts, the standard t-SNE loss (G1) is applied separately for each iteration t to preserve

semantic neighborhoods from the high-dimensional to the low-dimensional space per t . Specifically, Eq. (1) is used to compute the G1 loss, denoted as C_s , for each iteration independently as follows.

$$C_s = \frac{1}{T * N} \sum_t \text{KL}(P_t || Q_t) = \sum_t \sum_i \sum_{j, j \neq i} p_t^{ij} \ln \frac{p_t^{ij}}{q_t^{ij}} \quad (5)$$

C_s is normalized by the data size (N instances and T samples). Gradients $\partial C_s / \partial x_t^i$ and $\partial C_s / \partial y_t^i$ are computed as in the original paper [49].

Rectilinear Layout: models each iteration as a vertical line (see Fig. 1d). The low-dimensional elements \mathbf{I}_t^i , with coordinates (x_t^i, y_t^i) , are arranged along the x-axis according to their iteration t with the Cartesian displacement loss C_d^c (G2). C_d^c is designed as a Gaussian centered around an x-coordinate offset \bar{x}_t with a thickness determined by the Gaussians' standard deviation σ for each t in the low-dimensional space.

$$C_d^c = \frac{1}{T * N} \sum_t \sum_i C_d^c(i, t), \text{ where, } C_d^c(i, t) = \frac{1}{\sigma \sqrt{2\pi}} e^{-\frac{(x_t^i - \bar{x}_t)^2}{2\sigma^2}} \quad (6)$$

The Gaussian attracts elements at iteration t to \bar{x}_t , hence explicitly encoding iterations (see Fig. 3a). Initially, σ is set to a larger value σ_{start} to allow for more freedom in point movement, then reduced gradually to σ_{end} across optimization iterations to bring points closer to their corresponding \bar{x}_t . Vertical lines representing different iterations are positioned with a buffer spacing s between them. Noisy iterations are positioned on the left side.

The Cartesian alignment loss C_a^c (G3), aligns elements of each instance i across iterations. It is defined as the vertical distance between pairs of the same instance i across iterations consecutive t pair (see Eq. (7)) as in literature [4, 32]. Larger t values correspond to early generation steps. The cost and gradients are computed as follows,

$$C_a^c = \frac{1}{N * T} \sum_i \sum_{t=1}^T C_a^c(i, t), \text{ where, } C_a^c(i, t) = \|y_t^i - y_{t-1}^i\|^2 \quad (7)$$

$$\frac{\partial C}{\partial x_t^i} = \alpha * \frac{\partial C_s}{\partial x_t^i} + \beta * \frac{\partial C_d^c}{\partial x_t^i} \quad \frac{\partial C}{\partial y_t^i} = \alpha * \frac{\partial C_s}{\partial y_t^i} + \gamma * \frac{\partial C_a^c}{\partial y_t^i} \quad (8)$$

$$\frac{\partial C_d^c}{\partial x_t^i} = \frac{(x_t^i - \bar{x}_t)}{2\sigma^2} * C_d^c(i, t) \quad \frac{\partial C_a^c}{\partial y_t^i} = \frac{(y_t^i - y_{t+1}^i)}{C_a^c(i, t)}$$

The resultant force exerted on the data point \mathbf{I}_t^i by all three costs ($\partial C / \partial x_t^i$ and $\partial C / \partial y_t^i$) causes the points to move within the vertical band corresponding to iteration t . We initialize \mathbf{I}_t^i in a buffer region around the corresponding \bar{x}_t for faster optimization results. The expected result is that points are clustered based on semantic feature similarity around their corresponding x-offsets \bar{x}_t per iteration while maintaining the instance alignment across iterations (see Fig. 1).

Radial layout: The rectilinear layout fulfills our goals by enhancing the visualization of branching patterns and resembling the theoretical representation of expected behavior in Fig. 2. However, it uses space inefficiently, as all iterations are allocated equal space, even though early-generation steps, which are mostly noise, contain less relevant patterns. To address these gaps, we propose a radial layout with concentric rings (see Fig. 1d and Fig. 3b). Each iteration is represented as a ring; innermost rings show early noisy iterations and the outer rings show refined steps. Unlike the rectilinear layout, the radial layout optimizes space by assigning less area to early iterations and more to later ones. It also allows points to move flexibly around the rings, which may result in more effective embeddings.

The low-dimensional elements \mathbf{I}_t^i are represented in polar coordinates (r_t^i, θ_t^i) to facilitate the definition of forces in the radial layout.

Conceptually, the same losses C_s , C_d^c , and C_a^c are utilized, but the form is adapted to the radial layout. To preserve correctness of the Euclidean distance gradients in C_s , they are computed in Cartesian space and then converted to polar coordinates. The displacement loss (**G2**) was adapted for the radial layout C_d^p to organize elements of an iteration along the rings. It is modeled as a Gaussian centered around a radius-offset \bar{r}_t per iteration in the low-dimensional space in Eq. (9).

$$C_d^p = \frac{1}{T * N} \sum_t \sum_i C_d^p(i, t), \text{ where, } C_d^p(i, t) = -\frac{1}{\sigma\sqrt{2\pi}} e^{-\frac{(r_t^i - \bar{r}_t)^2}{2\sigma^2}}. \quad (9)$$

The Gaussian attracts elements at iteration t toward the corresponding ring center, \bar{r}_t (see Fig. 3b). The innermost ring corresponds to $\bar{r}_T = 0$, forming a circle. Subsequent rings have user-defined offsets $\bar{r}_{t=T} > 0$, which determine the spacing s between iterations as before.

The radial alignment loss (**G3**), C_a^p , ensures that elements of the same instance i across iterations are aligned, and it is defined as:

$$C_a^p = \frac{1}{N * T} \sum_i \sum_{t=1}^T 1 - |\text{sim}_t^i|, \text{ where, } \text{sim}_t^i = \cos\left(\frac{\theta_t^i - \theta_{t-1}^i}{2}\right). \quad (10)$$

We minimize the cosine distance between the angles θ_t^i of sequential pairs of corresponding elements. Halving the angular difference ensures the maximum cost is at π . We use the absolute value of cosine similarity to prevent poor local minima, particularly at π , where the angular difference is largest but the gradient of a cosine function is nearly flat. This could slow convergence when similar points are stuck on opposite sides. The optimization process follows a similar approach as the rectilinear one. However, in this case, the resultant force of the three cost elements leads to points moving along the respective iteration rings. The gradient updates in polar form are defined as follows:

$$\begin{aligned} \frac{\partial C_d^p}{\partial r_t^i} &= \frac{(r_t^i - \bar{r}_t)}{\sigma^2} * C_d^p(i, t) \\ \frac{\partial C_a^p}{\partial \theta_t^i} &= \begin{cases} -\frac{1}{2} \sin\left(\frac{\theta_t^i - \theta_{t-1}^i}{2}\right) & \text{if } \text{sim}_t^i < 0 \\ \frac{1}{2} \sin\left(\frac{\theta_t^i - \theta_{t-1}^i}{2}\right) & \text{if } \text{sim}_t^i > 0 \end{cases} \end{aligned} \quad (11)$$

The gradient of $\partial C_a^p / \partial \theta_t^i$ is undefined when $\text{sim}_t^i = 0$, where the point can move in either direction along the ring. While very unlikely to occur, we choose one of the two possible gradient directions randomly.

Note that the semantic C_s and displacement C_d in both layouts are inherently normalized as they are probability density functions (PDF). In rectilinear layouts, the vertical alignment loss C_a^c is min-max normalized per iteration. The angular alignment loss C_a^p in radial layouts is a scaled cosine loss $\in [0, 1]$, but becomes unbounded in Cartesian space. Since our optimization uses a fixed \bar{r}_t across t (later stretched for visualization), the costs remain consistent across datasets². While C_s^c and C_a^p are not PDFs, such joint optimizations are commonly performed in literature [4, 32], where variations in scales are managed through the weighting term; we follow this approach.

The choice of layout depends on the analytical objectives [27], with both offering distinct advantages and drawbacks. The rectilinear layout allocates equal space to all iterations, but not all layers have the same content in information. Early iterations often contain noisy, unstructured data, making it an inefficient use of space. In contrast, the radial layout optimizes space by allocating more room to later iterations, where more complex patterns emerge. While rectilinear layouts are useful for representing iterations, the main limitation, especially for representing semantic relations, is that elements at the extremes of the 1D-like embeddings can only show similarity in one direction (inward). The radial layout allows for movement along opposite directions of the cycle, so similar points can spread more naturally and easily across the ring. Further, the continuous, cyclic nature of this radial layout avoids extremes, offering a uniform interpretation and gradual evolution of all elements. Both layouts can provide complementary insights and may be analyzed side by side, depending on the application.

4.5 Interactive Front-End

As a proof-of-concept, we developed an interactive front-end² to explore data evolution within *EvolvED*. The evolutionary embedding is visualized in either radial or rectilinear layouts. When visualizing these embeddings to enable analysis, several considerations arise: 1) linking the embedding and the high-dimensional image space; 2) supporting analysis of the evolution of instances; and 3) characterizing images through prompt keyword-image links to improve comprehension of high-dimensional evolutionary data.

To comprehend the high-dimensional image space via the embedding, we display images of specific iterations (\mathbf{h}_{t-1}^i or $\mathbf{h}_{t_0}^i$) at regular intervals along the largest ring, spaced at intervals of θ degrees. The high-dimensional images \mathbf{h}_{t-1}^i or $\mathbf{h}_{t_0}^i$ of selected embedding elements are dynamically displayed for a linked analysis. To further explore the evolution and hierarchy of data, keywords or attributes within a prompt are utilized to color the low-dimensional embedding points. For example, a prompt “a dog on grass” can be colored by the keyword *dog* or *grass*, analyzing the effect of each keyword on the evolution process. To enhance the visualization of instance evolution, pathways connecting images of the same instance across iterations are traced with smooth curves. Given the potential for visual clutter arising from showing all pathways, we visualize only the evolution of selected elements \mathbf{h}_{t-1}^i of a specific instance i across iterations t (see Fig. 7). Simple data filters on the iteration step t , path lengths, and prompt keywords are provided to facilitate analysis. Users can interactively control keyword-color associations and pathway interpolation factors. It is important to note that our contribution primarily focuses on the *EvolvED* pipeline and evolutionary embedding rather than the interactive front-end aspect. We leave it to future work to achieve a complete visualization design.

5 EXPERIMENTS WITH EVOLVED COMPONENTS

Within *EvolvED*, several components interact, including the raw (intermediate) images, feature extractors, the evolutionary embedding and its loss functions. Understanding these interactions is crucial to elucidate how each component affects the outcomes of *EvolvED* and how it can be optimized for various cases. The below sections detail a simple example, the impact of the feature encoders, and adding constraints to t-SNE with our evolutionary embedding method.

5.1 Setup

We use GLIDE [26], a popular text-to-image diffusion model, for our experiments. We generate a set of 1000 samples from 10 randomly selected ImageNet classes as prompts \in [tiger, bird, car, fruit, building, dog, shark, ball, plane, table]. GLIDE’s base model was used to generate samples in 100 iterations. For the evolutionary embedding, 11 equally spaced iterations were used. Empirical findings suggested setting $\alpha = 1, \beta = 1$ and $\gamma = 0.05$, and $\gamma = 0.2$ for the rectilinear and radial layouts consistently yielded desired results. We use $\sigma_{start} = 20$, $\sigma_{end} = 10$ out $\bar{x}_t = \bar{r}_t = 20$, for optimization, stretched out with $s = 20$ for visualization across all our cases². We examine the impact of the interim images (\mathbf{h}_{t-1} , \mathbf{h}_{t_0}) encoded with different image encoders f to generate corresponding intermediate spaces. The evolutionary embedding is applied to this intermediate space and the raw images for comparison. The encoders explored include a robust ImageNet classifier [2] and the image encoder of CLIP [39]. CLIP is a foundational model that learns visual concepts from natural language supervision.

5.2 Impact of Image Encoders & Images Encoded

We evaluate the feature extractors affect *EvolvED* in generating embeddings from intermediate images of the diffusion process. Our goal is to assess the encoders’ effectiveness in extracting relevant semantic attributes while reflecting the inherent fuzziness of the images. We expect high levels of fuzziness in the high-dimensional images to result in mixed clusters across prompts in the early steps of the embedding, while later steps should produce distinct clusters as images improve.

Applying t-SNE to raw step-wise noisy (see Fig. 4a) and denoised images (see Fig. 4d) is a baseline for evaluating feature extractors.

²See supplementary materials for more details.

Figure 4 A1 shows that the noisy image colors can differ significantly at a pixel level, allowing their distinction in the embedding. However, with more nuanced semantic differences, raw image embeddings struggle to capture meaningful separation. When there are clearly semantic differences in images of birds, balls, or tigers in A3 and D1 (see Fig. 4), the raw image embeddings fail to differentiate these due to their reliance on pixel-level information. This shortcoming highlights the necessity of a feature extractor that go beyond raw pixel data to extract high-level semantic features for meaningful analysis.

We evaluate two feature extractors: a robust task-specific classifier trained on ImageNet [2] and the foundational, generic CLIP model [39], which is not explicitly trained to be robust. Both extractors provide more useful groupings in the embeddings compared to the raw image baseline in Fig. 4. Comparing the two, we observe that CLIP [39] struggles with noisy images in the early stages, as seen in Fig. 4 B1, where random images of dogs and cars are grouped together. However, by the final 30-40% of iterations, CLIP shows more useful groupings in B2, such as between tigers and dogs with a green background. In contrast, the robust classifier [2] excels even in the early-generation steps by reflecting image-level changes. For instance, Fig. 4 C1 shows that the classifier correctly groups dogs and tigers in a green background in the early stages, reflecting their shared contextual elements, whereas CLIP struggles to do the same. As the diffusion process progresses, the robust classifier maintains this contextual separation, resulting in well-defined clusters in Fig. 4 C2. Furthermore, in the very early stages (within the first 10% of iterations), the robust classifier differentiates images based on broad color differences, such as between the blue shark and red fruit classes. This confirms that a robust feature extractor works effectively even in the initial iterations of the diffusion process. While CLIP is not as effective as a robust classifier in the early stages, it still performs far better than the raw image baseline. This demonstrates the value of even a general-purpose extractor for noisy images, though robust models clearly offer an advantage.

When it comes to the step-wise denoised predictions at each iteration, the embeddings become clearer and more interpretable. Both the robust classifier (Fig. 4f) and CLIP (Fig. 4e) reflect the similarity between images in their embeddings. For example, when images are fuzzy in Fig. 4 E2 and F2, the embeddings reflect this with overlapping clusters, and they eventually separate these images as they become more distinct (E3 and F3). Images with distinct properties from the start, such as those in Fig. 4 E1 and F1, are separated early on. This demonstrates that both robust and general extractors work effectively on the step-wise denoised images, capturing the underlying semantic meaning.

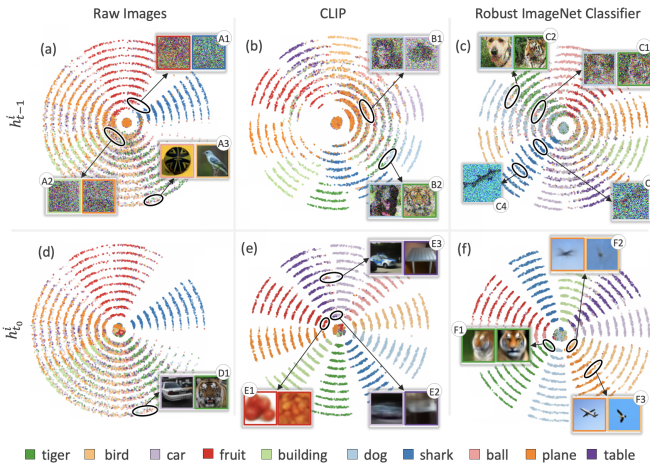


Fig. 4: Applying evolutionary embedding on GLIDE images with various feature extractors. (a) Noisy \mathbf{h}_{t-1} and (d) step-wise denoised images \mathbf{h}_{t_0} undergo evolutionary embedding. The noisy \mathbf{h}_{t-1} are encoded with (b) CLIP image encoder, and (c) a robust ImageNet classifier [2] before the embedding creation. Similarly, denoised \mathbf{h}_{t_0} are encoded with (e) a CLIP and (f) a robust ImageNet classifier.

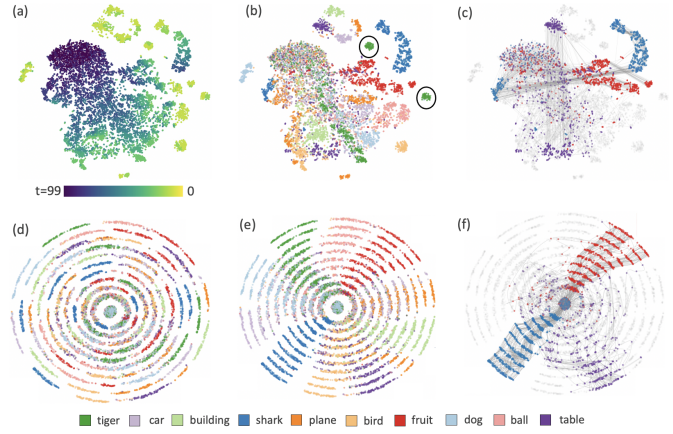


Fig. 5: Single vanilla t-SNE [49] embedding on all $\hat{\mathbf{h}}_{t-1}$ extracted from the GLIDE ImageNet use case with a classifier [2]. Points are colored by (a) iteration t and (b) prompt. Radial layout without (d) and with (e) the instance alignment loss. Pathways of “tables”, “sharks”, “fruits” are shown on the vanilla t-SNE (c) and radial layout (f).

In summary, robust feature extractors [2] work better for analyzing noisy images, while non-robust extractors [39] perform equally well with intermediate, denoised images. The choice of encoder is crucial for embedding quality; mismatches between the feature extractor and prompt focus can lead to ineffective embeddings. For example, an ImageNet classifier would not be ideal for analyzing medical images. While general-purpose models [39] outperform raw images, case-specific feature extractors, if available, are always preferable.

5.3 Evaluating Evolutionary Embedding

We explore each loss function Eq. (4), of our evolutionary embedding in Fig. 5 and compare the proposed layouts with with two baselines: 1) global vanilla t-SNE, embedding all steps t in a single space, and 2) step-wise vanilla t-SNE, creating separate embeddings for each t , i.e. C_s alone. We create embeddings of the step-wise noisy estimates \mathbf{h}_{t-1}^i encoded with an ImageNet classifier [2] for evaluation.

Global vanilla t-SNE enables analysis across steps, but as clusters become distinct, i.e., the yellow points of Fig. 5a, we lose the information about the progress through the iterations t , and about relations within iterations themselves. This makes it difficult to trace data evolution. Step-wise vanilla t-SNE offers better information within each iteration, but cluster evolution over time is difficult to trace, since each t is independent. The non-aligned iterations and the stochastic cluster placement complicate the tracing of data evolution. Our proposed radial layout in Fig. 5e explicitly encodes iterations and uses spatial coherence for analysis of cluster evolution patterns, something neither baseline achieves. For example, the early evolution of “shark” and “fruit” in Fig. 5f is not obvious in the global vanilla t-SNE in Fig. 5a and b. The radial layout (see Fig. 5d) reduces stochastic cluster placement (see Fig. 5e), while preserving cluster relations.

To evaluate the extent to which our added displacement and alignment constraints preserve high-dimensional neighborhoods, we compare our evolutionary embedding to the baselines using projection quality metrics, trustworthiness (Q_{trust}) and continuity (Q_{cont}) [16] per iteration t . These metrics take values in $[0, 1]$; one being the best performance. Q_{trust} checks whether the k nearest neighbors of an element remain neighbours in the high-dimensional space within an iteration. Q_{cont} checks whether the k nearest neighbors of an element in the high-dimensional space is preserved in the embedding. We utilize $k = 7$ neighbors inline with previous works [16, 24].

Q_{trust} and Q_{cont} for the proposed evolutionary embeddings remain comparable to full vanilla t-SNE in 6. While Q_{trust} of per step vanilla t-SNE is similar to our layouts, there is a minor deterioration in Q_{cont} in our layouts, primarily in early noisy steps, though they align better in later steps. This means that while the neighbors our layout shows are

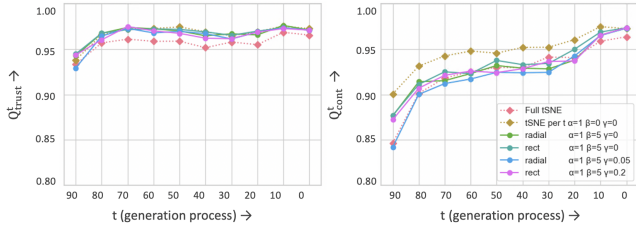


Fig. 6: Q_{trust}^t (left) and Q_{cont}^t (right) of full vanilla t-SNE across t , step-wise vanilla t-SNE per t (C_s), and the proposed radial (*radial*) and rectilinear (*rect*) layouts without (C_s with C_d) and with the alignment metric (C_s , C_d , and C_a) across iterations t . Embeddings are obtained on \hat{h}_{t-1}^i .

true, all neighbors cannot be preserved. This is expected, as step-wise vanilla t-SNE offers full 2D flexibility, while our method is constrained by a (narrow) Gaussian width per iteration, limiting how neighbors can be preserved. Further, there is minimal deterioration in both metrics when the alignment loss (C_a) is introduced Fig. 6, indicating that our method preserves high-dimensional structure while offering clearer insights into data evolution when compared to both baselines. Further, cluster quality metrics are comparable between the proposed radial and rectilinear layouts in Fig. 6. The main decline in quality metrics of the proposed radial method comes in the largest t value early in the generation process. Since these represent almost pure noise, so there is a lack of structure, the measures are of less relevance than the later generation steps. On the other hand, due to the limited one-directional movement in the rectilinear layout, alignment tends to work better with the radial layout, which offers more flexibility in the radial space². Finally, our method substantially reduces the computational time of global vanilla t-SNE ($> 9x$ per t) while providing more visual clarity of data evolution, which highlights both the efficiency and effectiveness of our approach. More analysis on embedding accuracy, displacement, and alignment losses are in the supplementary materials².

6 USE CASES

We demonstrate the potential of *EvolvED* by exploring various research questions, prompts, and diffusion models, to understand the generative process. We use both traditional (GLIDE [26]) and latent space (Stable Diffusion [41]) diffusion models. The first introductory case explores simple object evolution with GLIDE. The latter two explore nuanced feature evolution and prompt hierarchies across different hyperparameter settings using Stable Diffusion.

6.1 Exploring ImageNet Objects

In this section, we study the evolution of distinct high-level object types using 10 ImageNet classes, as described in Section 5.1. We start by analyzing the evolutionary embeddings of the noisy instances encoded with the robust classifier [2] in Fig. 7. Shorter paths indicate distinct modes, and the longer paths indicate branching and zig-zag patterns.

For instance, the *shark* and *fruit* classes exhibit shorter, more direct paths (red and blue points in Fig. 7a), which aligns with their distinct inner circle clusters in Fig. 4a due to their distinct colors. We also observe early differentiation in background features, such as grassy or watery environments, which further subdivide into sub-clusters like *dogs* and *tigers* on grass in Fig. 4 C2 and *sharks* in water in C4.

On exploring the longer paths shown in the rectilinear layout, we identify the *plane* class, since forming two clusters in the final step (Fig. 7b). Noisy images of planes are split based on the context. They are airborne (seen in the embedding close to birds) or grounded (seen in the embedding close to cars) in Fig. 7q and p. Clear distinctions is observed by the end, the earlier noisy images at $t = 40$ are seen as ambiguous, a pattern also noted in the CLIP-encoded features (Fig. 4b). In both cases, the visualization showed that the model seems to resolve context first, followed by finer details, providing an intuitive understanding of findings in literature [7, 38].

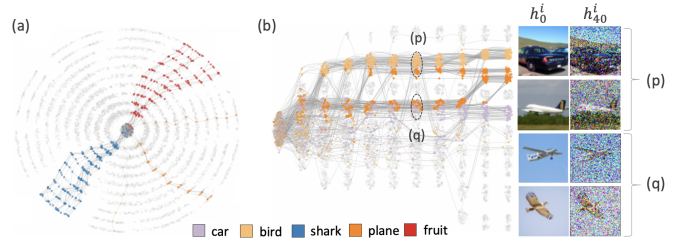


Fig. 7: Pathways of instances \hat{h}_{t-1}^i from GLIDE [26] encoded with an ImageNet classifier [2] traced in the evolutionary embeddings: (a) Pathways shorter than the 5th percentile in radial layout, primarily highlighting the *shark* and *fruit* instances. (b) Evolution of *plane* class and its clusters in the rectilinear layout, with images resembling *bird* or *car* at noisy $t=40$.

6.2 Exploring Human Facial Features

We explore the hierarchical evolution of features, identifying when and how they emerge during the generative process of Stable Diffusion [41]. This could help assess feature granularity, iteration redundancy, and refine model design. We also explore how hyperparameters, such as schedulers, influence data evolution. Our focus is data evolution in the context of human facial features, as this has been explored in literature [8]. With this research question, we design prompts that reflect varying levels of granularity in facial attributes. Our prompt is defined by the regular expression: “a photo of a [young | old] [man | woman]; with [brown | grey | blonde] hair; with [brown | blue] eyes; [wearing a necklace]?”. Images are generated in 40 iterations. We further sub-sample 11 iterations for the embedding and explore the attributes *age*, *gender*, and *haircolor*. This yielded a total of 48 prompts representing all possible keyword combinations defined above. 50 instances are sampled from each prompt for exploration. We choose CLIP to encode attributes of interest, as it has been shown to work with generic facial attributes in previous studies [1].

Feature evolution: We analyze the progression of facial feature clusters during the diffusion process. Early on, in the third ring, *gender* forms clear clusters, with pink (female) and purple (male) points separating in Fig. 8a. By the fourth ring, age-related clusters emerge, with clear separations between younger (light orange) and older (dark green) people in Fig. 8b. This is reflected in the denoised image estimates, where age related characteristics emerge over time. The rectilinear layout in Fig. 8a shows clearer early separations due to space but struggles with complex relations because of its one-directional similarity limit, whereas the radial layout in Fig. 8b works better for this, highlighting the value of joint analysis.

Hair color clusters show a different pattern; they remain mixed for older people, particularly in Fig. 8c1, reflecting a feature entanglement, i.e., *old* individuals with *brown* or *blonde* hair often blend into *grey*. For younger people, distinct hair color clusters appear halfway through the process ($c4$ and $c7$), though some mixing between green and blue points occurs for males in the bottom quartile of Fig. 8, likely due to subjective differences in dark blonde vs. brunette or hair volume. Further, *grey* hair clusters isolate faster than *blonde* or *brown*, as shown by the distinct separation in $c6$ versus the mixed grouping in $c3$. This is mirrored in the denoised images, where *brown* hair in earlier steps resembles a darker blonde.

This feature progression demonstrates the diffusion model’s ability to capture low-frequency features like gender early on and later focus on higher-frequency details, a finding consistent with literature [8, 38]. *EvolvED* provides an intuitive way to pinpoint when specific features emerge and how they compare to others, a capability that is difficult to achieve with existing methods due to their lack of coherence and limited ability to explore trends across iterations.

Exploring schedulers: The evolution of features in diffusion models depends significantly on the model, hyperparameters, and schedulers used. Schedulers control how noise is added and removed



Fig. 8: Evolution of human facial attributes with Stable Diffusion and varying schedulers. CLIP representations of the step-wise denoised images $\hat{\mathbf{h}}_{t_0}$ are summarized with the evolutionary embedding and color-encoded to show (a) *gender*, (b) *age*, and (c) *hair color*, with data generated using a DDPM scheduler. The same embedding is generated for the EulerA scheduler. The evolution of young *brown*, *blonde*, *grey* hair (denoised) images is compared between DDPM (C2-C7) and EulerA (D2-D7). Mixed hair clusters for older people are indicated in both scheduler embeddings (C1, D1).

during generation, influencing image quality, diversity, and speed. Understanding their impact is a critical area of research [9]. We compare two popular schedulers: DDPM (Denoising Diffusion Probabilistic Model) and Euler Ancestral Discrete Sampling (EulerA). DDPM removes noise in small, linear steps, while EulerA takes larger steps initially but converges faster, leading to more diverse and higher-quality outputs. Visualizing the step-by-step evolution of hair color clusters with *EvolvED*, sheds light on how schedulers manage image-clarity and diversity trade-offs (see Fig. 8c and d).

The DDPM embedding shows gradually emerging clusters (see Fig. 8 c2 evolving into c3, c4, and c5), which mirrors the gradual changes in the denoised images (see Fig. 8c2-c4). In contrast, EulerA embedding displays chaotic, mixed clusters for the first 40% of steps, as evident from the disordered colors up to the fourth ring (see Fig. 8d). We observe that while DDPM gradually refines clusters, EulerA begins with disordered clusters that only start to separate around the fourth ring. This chaotic behavior in EulerA is reflected in the unstructured, poorly denoised images during early generative steps (see Fig. 8d2, d3), indicating the model’s limited knowledge of the final image at that stage. However, this flexibility likely allows EulerA to generate more diverse outputs. After this early stage, EulerA converges quickly, producing clearer clusters and sharper, vibrant images in fewer steps in Fig. 8d4 compared to DDPM in c4. This chaotic start and quick convergence in the embedding overview clearly represents the detailed image-level changes, highlighting the usefulness of *EvolvED* to study data evolution holistically.

This analysis, enabled by *EvolvED*, pinpoints key moments when features emerge and refine, offering valuable insights into how each scheduler manages the clarity-diversity tradeoff. While current work on schedulers [23] look at aggregate noise-level changes, it lacks direct exploration of their impact on high-dimensional data. *EvolvED* fills this gap by visualizing feature evolution, providing practical insights into how schedulers influence outputs beyond noise scales. Tracking feature evolution helps identify critical refinement stages, which could guide scheduler design or distillation [23].

6.3 Exploring Image Styles

We shift our research question to explore how hierarchical prompts influence the generative process and pathways within Stable Diffusion [41]. Specifically, do generic prompts lead to broader evolutions that encompass those of specific prompts. We investigate the evolution of (cat) image styles, explored in literature [18]. Our goal is to analyze how prompt specificity influences generative pathways, shedding light on learned distributions, potential entanglements, and guiding data generation strategies. For this purpose, we tailor our prompts as, “A [realistic photo of a | painting of a] [domestic | wild]? cat [in the cubism style | in the renaissance style]?”. We sampled 100 instances from each combination. We apply CLIP on the denoised estimates \mathbf{h}_{t_0} , which were then summarized through our evolutionary

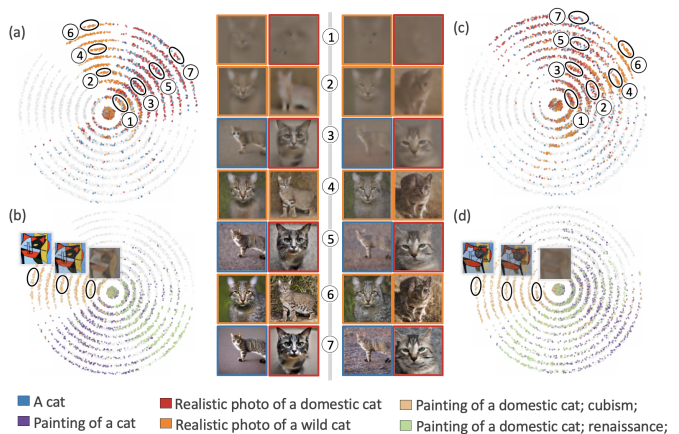


Fig. 9: Effect of prompt specificity and guidance scale on data evolution in StableDiffusion. Scale is 7.5 in (a), (b) and 3 in (c), (d). The evolutionary embedding is based on denoised representations (a) The evolution of “a cat” and “a realistic photo of a domestic cat”, which follow similar paths, while “wild cat” images form distinct clusters. (b) Painting styles like cubism and renaissance diverge early. Reducing guidance scale in (c), (d) lead to more variability in domestic cat images, now exhibiting wild features, while cubism and wild cat pathways remain stable.

embedding method. CLIP was selected for its applicability in style transfer tasks [31] and generic object-encoding capability, inline with our focus.

Prompt Specificity & Generation Pathways: Figure 9a shows an interesting pattern: blue points representing the prompt “a cat” follow almost identical evolution paths as red points representing “a realistic photo of a domestic cat”. The images also indicate that both prompts predominantly generate similar domestic cat (denoised) images (see 9a1, a3, a5, a7). In contrast, *wild* cats evolve along a distinct path, with clear clusters in 9 a2 and a4. While initially mixed with domestic cats (see Fig. 9a1), wild cat features like pointy ears and stretched faces begin to emerge (see Fig. 9a2) in the denoised images, 30% into the generation process. These features set them apart from the softer features of domestic cat (denoised) images in 9a3. Analyzing this encompassing aspect of prompts allows us to understand their generated distributions. In our case, this suggests a skew of cat images toward domestic cats, potentially reflecting the composition of its training data. On the other hand, *paintings* can be seen to evolve differently (see Fig. 9b) from the *photos*, as expected. Notably, cubism-style paintings take on a unique trajectory, separating early in the generative process (around 20% into generation), likely

due to their bold color patterns. This early separation shown in the embedding suggests that specific prompts, such as artistic styles, can guide the generation process toward more distinct outputs, which could be important when aiming for highly specific image characteristics.

Impact of guidance scale: Next, we analyze the guidance scale, as prompt specificity alone may not control image diversity. The guidance scale influences how closely the model follows the text prompt. By adjusting it, we can explore with *EvolveD* how generation pathways shift and whether this leads to more flexible or precise outputs, such as combining the domestic and wild cat pathways better.

In Fig. 9c and Fig. 9d, we lowered the guidance scale from 7.5 to 3 to observe its impact on the generative process. With less guidance, *EvolveD*'s data evolution visualization helps reveal widened variability from the get go in both the embedding and in the denoised images of the prompts "a cat" and "a domestic cat". For instance, in Fig. 9c7, what were previously more controlled domestic cat-like images (see Fig. 9a7) now exhibit features like nature backgrounds and textured coats, indicating more diverse outputs, reflected by the partial pathway overlap between *domestic* and *wild* cats. Despite this increased variability, the embedding shows that domestic and wild cat prompts follow (less) distinct pathways (see Fig. 9c4-7). It also revealed persistent underlying entanglements between photos of cats and domestic cats (Fig. 9c3-7). This deep entanglement becomes clear through the full process visualization provided by *EvolveD*. Further, the effect of reducing the guidance scale varies across prompts. For domestic cats, clusters emerge more slowly, as seen in the more fuzzy denoised images in Fig. 9c2, c4, and c6, compared to earlier formations in Fig. 9a. However, wild cats (Fig. 9a2-a6 vs. c2-c6) and cubism paintings are less affected by the reduced guidance (Fig. 9b vs. d), maintaining stable generative pathways. This variability in prompt responses to guidance adjustments was made evident through *EvolveD*'s ability to track feature progression over time.

Generic prompts revealed distribution biases (domestic cat vs. cat), and did not fully encompass specific prompts. The differences in how guidance scales affect the output may stem from the internal model specificity of certain prompts, which retain consistent generative modes, explaining why cubism paintings show less variability. *EvolveD* was useful in visualizing how prompt specificity and guidance levels influence generation, offering insights beyond what static outputs can reveal. This understanding could inform improvements in training distributions, model adjustments, and better control over generative pathways.

7 DISCUSSIONS

EvolveD: While our focus was the evolution of higher-level semantic features like *hair color* in intermediate diffusion images, other evolution dimensions can also be explored, such as U-Net model features [8], or concept-keyword associations [28]. Exploring the U-Net features is not straightforward since they do not have a unified latent layer, owing to their skip connections, and different layers being important in different iterations [38, 43]. Next, developing advanced visual and interactive design could enhance the analysis of the evolutionary embedding layout generated by *EvolveD*. For example, better edge bundling methods could allow the evolution of modes to be less cluttered. Images visualized on the outer portions of the layouts could be sampled to be better representatives of the respective cluster. Additionally, techniques like word cloud embedding could support the exploration of complex prompt sets.

Evolutionary Embedding: We implement the evolutionary embedding with vanilla t-SNE [49] as a proof of concept. While faster t-SNE [35, 36] or UMAP [22] should work conceptually since we only add loss functions, we leave this to future work. We empirically identified a set of weights the three losses for each layout that performed consistently well across our cases. However, their weighting balance needs to be considered based on new case requirements. For our alignment constraint, we explore a pairwise loss across consecutive iterations as in prior works [4]. However, this can be improved via

a global alignment across iterations. While rectilinear and radial layouts offer distinct advantages, a formal evaluation of these layouts for representing semantic relations in this context as developed in literature [27] may be useful in future work. Next, we used Euclidean distances for C_s in the low-dimensional space of the radial layout. While empirically, this form was still found to work well, C_s does not follow the ring structure of the layout and hence can be improved. A polar-space alternative for C_s could improve optimization but presents challenges for maintaining gradient correctness.

Scalability: Diffusion models consist of several iterations, in the order of 1000. While popular methods [26, 41] reduce this to < 100 , the size remains substantial for visualization. This challenge is particularly observed in radial layouts, where the inner circles are allotted less space. We sub-sampled iterations in an evenly spaced manner to mitigate visualization difficulties. However, more effective interactive sampling methods or hierarchical dimensionality reduction [33] can be used. Finally, the evolution of only a few attributes can be studied at a single time due to limitations in the number of colors used to encode data attributes like *hair color* discernible by the human eye. While we reduce this variability with the research question, there is a need for sequential prioritization and analysis of attributes in the current setting.

Future Applications: While the main focus of *EvolveD* is to support an understanding of data evolution of diffusion models, its applicability extends to several practically-oriented downstream tasks. First, exploring branching patterns and when dataset modes emerge are relevant for designing architectures, noise schedulers, and distillation methods [9, 15, 23]. If all modes of interest manifest in early iterations, the number of iterations could be reduced [7]. *EvolveD* serves as a valuable tool for visualizing attribute entanglements [52, 54] and an evolution level. Extensions of *EvolveD* could support interactive data generation processes to help users understand and control the generation process. Lastly, the proposed evolutionary embedding can be extended to diffusion models beyond text-to-image, general DL models feature evolution, model training evolution, and potentially other (non-image) high-dimensional evolutionary data.

8 CONCLUSIONS

Diffusion models iteratively reconstruct corrupted data, iteratively evolving noisy images into refined outputs. Understanding this data evolution is essential for model understanding and development, but remains complex due to its high-dimensional and iterative nature. Existing methods focus on single-step or instance analyses, and do not look at the holistic and iterative aspects together. Hence we propose the *EvolveD*, a method for holistically understanding data evolution in the generative process of diffusion models. *EvolveD* samples the generative space by extracting instances across focused prompts and employs feature extractors to isolate specific attributes from intermediate images, preserving the iterative context. An evolutionary embedding method is introduced to explicitly encode iterations context while maintaining the feature relations and their evolution to enable analysis. Our embedding method achieves this by three main goals: grouping semantically similar elements, organizing elements by iteration, and aligning an instance's elements across iterations. This embedding allows us to visualize data evolution in rectilinear and radial layouts, offering a view of the model's progression over time. With different research questions and prompts, we show the versatility and value of *EvolveD* by applying it to two prominent text-to-image diffusion models, GLIDE and StableDiffusion. *EvolveD* serves as a powerful tool for analyzing data evolution in diffusion models, with applications in understanding feature progression, distributions, and potentially guiding their design.

REFERENCES

- [1] S. Agarwal, G. Krueger, J. Clark, A. Radford, J. W. Kim, and M. Brundage. Evaluating clip: towards characterization of broader capabilities and downstream implications. *arXiv preprint arXiv:2108.02818*, 2021. 7

- [2] Y. Bai, J. Mei, A. L. Yuille, and C. Xie. Are transformers more robust than cnns? In M. Ranzato, A. Beygelzimer, Y. Dauphin, P. Liang, and J. W. Vaughan, eds., *Advances in Neural Information Processing Systems*, vol. 34, pp. 26831–26843. Curran Associates, Inc., 2021. doi: 10.48550/arXiv.2111.05464 1, 3, 5, 6, 7
- [3] G. D. Cantareira, R. F. Mello, and F. V. Paulovich. Explainable adversarial attacks in deep neural networks using activation profiles. *arXiv preprint arXiv:2103.10229*, 2021. doi: 10.48550/arXiv.2103.10229 3
- [4] G. D. Cantareira and F. V. Paulovich. A Generic Model for Projection Alignment Applied to Neural Network Visualization. In C. Turkay and K. Vrotsou, eds., *EuroVis Workshop on Visual Analytics (EuroVA)*. The Eurographics Association, 2020. doi: 10.2312/eurova.20201089 3, 4, 5, 9
- [5] Z. Chang, G. A. Koulouris, and H. P. Shum. On the design fundamentals of diffusion models: A survey. *arXiv preprint arXiv:2306.04542*, 2023. doi: 10.48550/arXiv.2306.04542 2
- [6] H. Chefer, Y. Alaluf, Y. Vinker, L. Wolf, and D. Cohen-Or. Attend-and-excite: Attention-based semantic guidance for text-to-image diffusion models. *ACM Transactions on Graphics*, 42(4), article no. 148, 10 pages, jul 2023. doi: 10.1145/3592116 3
- [7] K. Deja, A. Kuzina, T. Trzcinski, and J. Tomczak. On analyzing generative and denoising capabilities of diffusion-based deep generative models. In S. Koyejo, S. Mohamed, A. Agarwal, D. Belgrave, K. Cho, and A. Oh, eds., *Advances in Neural Information Processing Systems*, vol. 35, pp. 26218–26229. Curran Associates, Inc., 2022. doi: 10.48550/arXiv.2206.00070 1, 2, 7, 9
- [8] K. Deja, T. Trzcinski, and J. M. Tomczak. Learning data representations with joint diffusion models. In D. Koutra, C. Plant, M. Gomez Rodriguez, E. Baralis, and F. Bonchi, eds., *Machine Learning and Knowledge Discovery in Databases: Research Track*, pp. 543–559. Springer Nature Switzerland, Cham, 2023. doi: 10.1007/978-3-031-43415-0_32 7, 9
- [9] Z. Duan, C. Wang, C. Chen, J. Huang, and W. Qian. Optimal linear subspace search: Learning to construct fast and high-quality schedulers for diffusion models. In *Proceedings of the 32nd ACM International Conference on Information and Knowledge Management*, pp. 463–472, 2023. 1, 8, 9
- [10] Y. Fang, H. Xu, and J. Jiang. A survey of time series data visualization research. *IOP Conference Series: Materials Science and Engineering*, 782(2):022013, mar 2020. doi: 10.1088/1757-899X/782/2/022013 3
- [11] A. Hertz, R. Mokady, J. Tenenbaum, K. Aberman, Y. Pritch, and D. Cohen-Or. Prompt-to-prompt image editing with cross attention control. *arXiv preprint arXiv:2208.01626*, 2022. doi: 10.48550/arXiv.2208.01626 3
- [12] A. Hinterreiter, C. Steinparz, M. Schöfl, H. Stitz, and M. Streit. Projection path explorer: Exploring visual patterns in projected decision-making paths. *ACM Trans. Interact. Intell. Syst.*, 11(3–4), article no. 22, 29 pages, sep 2021. doi: 10.1145/3387165 3
- [13] J. Ho, A. Jain, and P. Abbeel. Denoising diffusion probabilistic models. In H. Larochelle, M. Ranzato, R. Hadsell, M. Balcan, and H. Lin, eds., *Advances in Neural Information Processing Systems*, vol. 33, pp. 6840–6851. Curran Associates, 2020. doi: 10.48550/arXiv.2006.11239 2
- [14] M. Kahng, N. Thorat, D. H. Chau, F. B. Viégas, and M. Wattenberg. Gan lab: Understanding complex deep generative models using interactive visual experimentation. *IEEE Transactions on Visualization and Computer Graphics*, 25(1):310–320, 2019. doi: 10.1109/TVCG.2018.2864500 3
- [15] T. Karras, M. Aittala, T. Aila, and S. Laine. Elucidating the design space of diffusion-based generative models. *Advances in Neural Information Processing Systems*, 35:26565–26577, 2022. doi: 10.48550/arXiv.2206.00364 1, 9
- [16] S. Kaski, J. Nikkilä, M. Oja, J. Venna, P. Törönen, and E. Castrén. Trustworthiness and metrics in visualizing similarity of gene expression. *BMC bioinformatics*, 4:1–13, 2003. doi: 10.1186/1471-2105-4-48 6
- [17] M. Kwon, J. Jeong, and Y. Uh. Diffusion models already have a semantic latent space. In *The Eleventh International Conference on Learning Representations*, 2023. doi: 10.48550/arXiv.2210.10960 3
- [18] S. Lee, B. Hoover, H. Strobelt, Z. J. Wang, S. Peng, A. Wright, K. Li, H. Park, H. Yang, and D. H. Chau. Diffusion explainer: Visual explanation for text-to-image stable diffusion. *arXiv preprint arXiv:2305.03509*, 2023. doi: 10.48550/arXiv.2305.03509 2, 3, 8
- [19] M. Li, Z. Zhao, and C. Scheidegger. Visualizing neural networks with the grand tour. *Distill*, 5(3):e25, 2020. 3
- [20] S. Luccioni, C. Akiki, M. Mitchell, and Y. Jernite. Stable bias: Evaluating societal representations in diffusion models. In *Thirty-seventh Conference on Neural Information Processing Systems Datasets and Benchmarks Track*, 2023. doi: 10.48550/arXiv.2303.11408 3
- [21] Q. Luo, L. Christino, F. V. Paulovich, and E. Milios. Dimenfix: A novel meta-dimensionality reduction method for feature preservation. *arXiv preprint arXiv:2211.16752*, 2022. doi: 10.48550/arXiv.2211.16752 3
- [22] L. McInnes, J. Healy, N. Saul, and L. Großberger. Umap: Uniform manifold approximation and projection. *Journal of Open Source Software*, 3(29):861, 2018. doi: 10.21105/joss.00861 2, 9
- [23] C. Meng, R. Rombach, R. Gao, D. Kingma, S. Ermon, J. Ho, and T. Salimans. On distillation of guided diffusion models. In *Proceedings of the IEEE/CVF Conference on Computer Vision and Pattern Recognition*, pp. 14297–14306, 2023. 1, 3, 8, 9
- [24] L. Meng, S. van den Elzen, N. Pezzotti, and A. Vilanova. Class-constrained t-sne: Combining data features and class probabilities. *IEEE Transactions on Visualization and Computer Graphics*, 30(1):164–174, 2024. doi: 10.1109/TVCG.2023.3326600 6
- [25] A. Q. Nichol and P. Dhariwal. Improved denoising diffusion probabilistic models. In *International Conference on Machine Learning*, pp. 8162–8171. PMLR, 2021. doi: 10.48550/arXiv.2102.09672 2
- [26] A. Q. Nichol, P. Dhariwal, A. Ramesh, P. Shyam, P. Mishkin, B. McGrew, I. Sutskever, and M. Chen. GLIDE: Towards photorealistic image generation and editing with text-guided diffusion models. In *Proceedings of the 39th International Conference on Machine Learning*, Proceedings of Machine Learning Research. PMLR, 2022. doi: 10.48550/arXiv.2112.10741 1, 2, 5, 7, 9
- [27] A. Pandey, S. L’Yi, Q. Wang, M. A. Borkin, and N. Gehlenborg. Genorec: a recommendation system for interactive genomics data visualization. *IEEE transactions on visualization and computer graphics*, 29(1):570–580, 2022. 4, 5, 9
- [28] J.-H. Park, Y.-J. Ju, and S.-W. Lee. Explaining generative diffusion models via visual analysis for interpretable decision-making process. *Expert Systems with Applications*, 248:123231, 2024. doi: 10.1016/j.eswa.2024.123231 1, 2, 3, 9
- [29] Y.-H. Park, M. Kwon, J. Choi, J. Jo, and Y. Uh. Understanding the latent space of diffusion models through the lens of riemannian geometry. In A. Oh, T. Neumann, A. Globerson, K. Saenko, M. Hardt, and S. Levine, eds., *Advances in Neural Information Processing Systems*, vol. 36, pp. 24129–24142. Curran Associates, Inc., 2023. doi: 10.48550/arXiv.2307.12868 1, 3
- [30] G. Parmar, K. Kumar Singh, R. Zhang, Y. Li, J. Lu, and J.-Y. Zhu. Zero-shot image-to-image translation. In *ACM SIGGRAPH 2023 Conference Proceedings*, SIGGRAPH ’23, article no. 11, 11 pages. Association for Computing Machinery, New York, NY, USA, 2023. doi: 10.1145/3588432.3591513 3
- [31] O. Patashnik, Z. Wu, E. Shechtman, D. Cohen-Or, and D. Lischinski. Styleclip: Text-driven manipulation of stylegan imagery. In *Proceedings of the IEEE/CVF international conference on computer vision*, pp. 2085–2094, 2021. 8
- [32] N. Pezzotti, J.-D. Fekete, T. Höllt, B. P. Lelieveldt, E. Eisemann, and A. Vilanova. Multiscale visualization and exploration of large bipartite graphs. In *Computer Graphics Forum*, vol. 37, pp. 549–560. Wiley Online Library, 2018. doi: 10.1111/cgf.13441 3, 4, 5
- [33] N. Pezzotti, T. Höllt, B. Lelieveldt, E. Eisemann, and A. Vilanova. Hierarchical stochastic neighbor embedding. In *Computer Graphics Forum*, vol. 35, pp. 21–30. Wiley Online Library, 2016. doi: 10.1111/cgf.12878 9
- [34] N. Pezzotti, T. Höllt, J. Van Gemert, B. P. Lelieveldt, E. Eisemann, and A. Vilanova. Deepeyes: Progressive visual analytics for designing deep neural networks. *IEEE Transactions on Visualization and Computer Graphics*, 24(1):98–108, 2018. doi: 10.1109/TVCG.2017.2744358 3
- [35] N. Pezzotti, B. P. F. Lelieveldt, L. v. d. Maaten, T. Höllt, E. Eisemann, and A. Vilanova. Approximated and user steerable tsne for progressive visual analytics. *IEEE Transactions on Visualization and Computer Graphics*, 23(7):1739–1752, 2017. doi: 10.1109/TVCG.2016.2570755 9
- [36] N. Pezzotti, J. Thijssen, A. Mordvintsev, T. Höllt, B. Van Lew, B. P. Lelieveldt, E. Eisemann, and A. Vilanova. Gpgpu linear complexity t-sne optimization. *IEEE Transactions on Visualization and Computer Graphics*, 26(1):1172–1181, 2020. doi: 10.1109/TVCG.2019.2934307 9
- [37] V. Prasad, R. J. van Sloun, S. van den Elzen, A. Vilanova, and N. Pezzotti. The transform-and-perform framework: Explainable deep learning beyond classification. *IEEE Transactions on Visualization and Computer Graphics*, 30(2):1502–1515, 2022. doi: 10.1109/TVCG.2022.3219248 1, 3
- [38] V. Prasad, C. Zhu-Tian, A. Vilanova, H. Pfister, N. Pezzotti, and H. Strobelt. Unraveling the temporal dynamics of the unet in diffusion models, 2024. doi: 10.48550/arXiv.2312.14965 1, 2, 3, 7, 9

- [39] A. Radford, J. W. Kim, C. Hallacy, A. Ramesh, G. Goh, S. Agarwal, G. Sastry, A. Askell, P. Mishkin, J. Clark, et al. Learning transferable visual models from natural language supervision. In *International conference on machine learning*, pp. 8748–8763. PMLR, 2021. doi: 10.48550/arXiv.2103.00020 3, 5, 6
- [40] P. E. Rauber, S. G. Fadel, A. X. Falcão, and A. C. Telea. Visualizing the hidden activity of artificial neural networks. *IEEE Transactions on Visualization and Computer Graphics*, 23(1):101–110, 2017. doi: 10.1109/TVCG.2016.2598838 3
- [41] R. Rombach, A. Blattmann, D. Lorenz, P. Esser, and B. Ommer. High-resolution image synthesis with latent diffusion models. In *Proceedings of the IEEE/CVF Conference on Computer Vision and Pattern Recognition (CVPR)*, pp. 10684–10695, June 2022. doi: 10.1109/CVPR52688.2022.01042 2, 3, 7, 8, 9
- [42] O. Ronneberger, P. Fischer, and T. Brox. U-net: Convolutional networks for biomedical image segmentation. In N. Navab, J. Hornegger, W. M. Wells, and A. F. Frangi, eds., *Medical Image Computing and Computer-Assisted Intervention*, pp. 234–241. Springer, Cham, 2015. doi: 10.1007/978-3-319-24574-4_28 1, 2
- [43] C. Si, Z. Huang, Y. Jiang, and Z. Liu. Freeu: Free lunch in diffusion u-net. *arXiv preprint arXiv:2309.11497*, 2023. doi: 10.48550/arXiv.2309.11497 1, 2, 9
- [44] J. Sohl-Dickstein, E. Weiss, N. Maheswaranathan, and S. Ganguli. Deep unsupervised learning using nonequilibrium thermodynamics. In *International conference on machine learning*, pp. 2256–2265. PMLR, 2015. doi: 10.48550/arXiv.1503.03585 2
- [45] Y. Song, J. Sohl-Dickstein, D. P. Kingma, A. Kumar, S. Ermon, and B. Poole. Score-based generative modeling through stochastic differential equations. In *International Conference on Learning Representations*, 2021. doi: 10.48550/arXiv.2011.13456 2, 3
- [46] R. Tang, L. Liu, A. Pandey, Z. Jiang, G. Yang, K. Kumar, P. Stenetorp, J. Lin, and F. Ture. What the DAAM: Interpreting stable diffusion using cross attention. In A. Rogers, J. Boyd-Graber, and N. Okazaki, eds., *Proceedings of the 61st Annual Meeting of the Association for Computational Linguistics*, pp. 5644–5659. Association for Computational Linguistics, Toronto, Canada, July 2023. doi: 10.18653/v1/2023.acl-long.310 3
- [47] N. Tumanyan, M. Geyer, S. Bagon, and T. Dekel. Plug-and-play diffusion features for text-driven image-to-image translation. In *2023 IEEE/CVF Conference on Computer Vision and Pattern Recognition (CVPR)*, pp. 1921–1930, 2023. doi: 10.1109/CVPR52729.2023.00191 3
- [48] A. Vahdat, K. Kreis, and J. Kautz. Score-based generative modeling in latent space. *Advances in neural information processing systems*, 34:11287–11302, 2021. doi: 10.48550/arXiv.2106.05931 3
- [49] L. van der Maaten and G. Hinton. Visualizing data using t-sne. *Journal of Machine Learning Research*, 9(86):2579–2605, 2008. 2, 4, 6, 9
- [50] M. Videau, N. Knizev, A. Leite, M. Schoenauer, and O. Teytaud. Interactive latent diffusion model. In *Proceedings of the Genetic and Evolutionary Computation Conference, GECCO '23*, 11 pages, p. 586–596. Association for Computing Machinery, New York, NY, USA, 2023. doi: 10.1145/3583131.3590471 2
- [51] Z. J. Wang, R. Turko, O. Shaikh, H. Park, N. Das, F. Hohman, M. Kahng, and D. H. Polo Chau. Cnn explainer: Learning convolutional neural networks with interactive visualization. *IEEE Transactions on Visualization and Computer Graphics*, 27(2):1396–1406, 2021. doi: 10.1109/TVCG.2020.3030418 3
- [52] Q. Wu, Y. Liu, H. Zhao, A. Kale, T. Bui, T. Yu, Z. Lin, Y. Zhang, and S. Chang. Uncovering the disentanglement capability in text-to-image diffusion models. In *2023 IEEE/CVF Conference on Computer Vision and Pattern Recognition*, pp. 1900–1910. IEEE Computer Society, Los Alamitos, CA, USA, jun 2023. doi: 10.1109/CVPR52729.2023.00189 1, 9
- [53] L. Yang, Z. Zhang, Y. Song, S. Hong, R. Xu, Y. Zhao, W. Zhang, B. Cui, and M.-H. Yang. Diffusion models: A comprehensive survey of methods and applications. *ACM Computing Surveys*, 56(4), article no. 105, 39 pages, nov 2023. doi: 10.1145/3626235 1
- [54] T. Yang, Y. Wang, Y. Lu, and N. Zheng. Disdiff: Unsupervised disentanglement of diffusion probabilistic models. In *Thirty-seventh Conference on Neural Information Processing Systems*, 2023. doi: 10.48550/arXiv.2301.13721 1, 3, 9
- [55] Y. Zhao, M. Li, and M. Berger. Cupid: Contextual understanding of prompt-conditioned image distributions. In *Computer Graphics Forum*, p. e15086. Wiley Online Library, 2024. 3

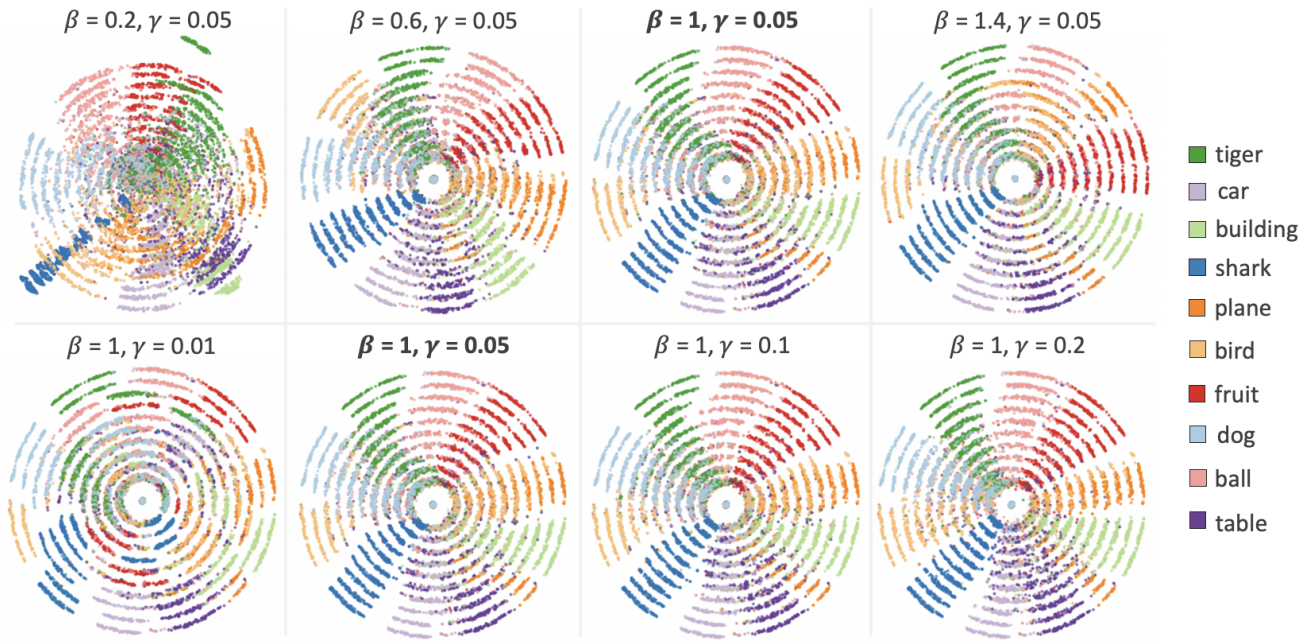


Fig. 10: **Exploring different β and γ weightings for the radial layout losses C_d^p and C_a^p respectively, with $\alpha = 1$.** When $\beta = 0.2$, the iterations are poorly separated. Increasing $\beta = 0.6$ enhances separation, yet inner clusters remain insufficiently distinguished. While $\beta \in \{1, 1.4\}$, the iterations display well-defined separation. $\beta = 1$ is chosen to maintain the t-SNE cluster structure while meeting our objectives. Similarly, with $\gamma = 0.01$, points demonstrate poor alignment, hindering the exploration of data evolution. Increasing γ values of 0.05 and 0.1 leads to sufficient alignment. $\gamma = 0.05$ is selected based on the above insights and neighborhood quality metrics. All embeddings in this document are on the ImageNet objects case, where the noisy representations \hat{h}_i^t ($t = 99$ to $t = 0$) are first encoded with a classifier. While the cosine alignment C_a loss is normalized $([0, 1])$, converting it back into Cartesian coordinates for gradient updates causes the step sizes to vary depending on the radius size, as angular distances change in the Euclidean space across radii. To accommodate t-SNE, which optimizes better when points are closer to the center, we use a fixed radius of $\bar{r}_t = 20$ across iterations for optimization and stretch out the radii for visualization; our chosen $\gamma = 0.05$ is based on this. Changing \bar{r}_t is expected to influence γ and requires careful tuning. Since $\bar{r}_t = 20$ has been empirically verified to work well with t-SNE, we recommend maintaining this value for optimization.

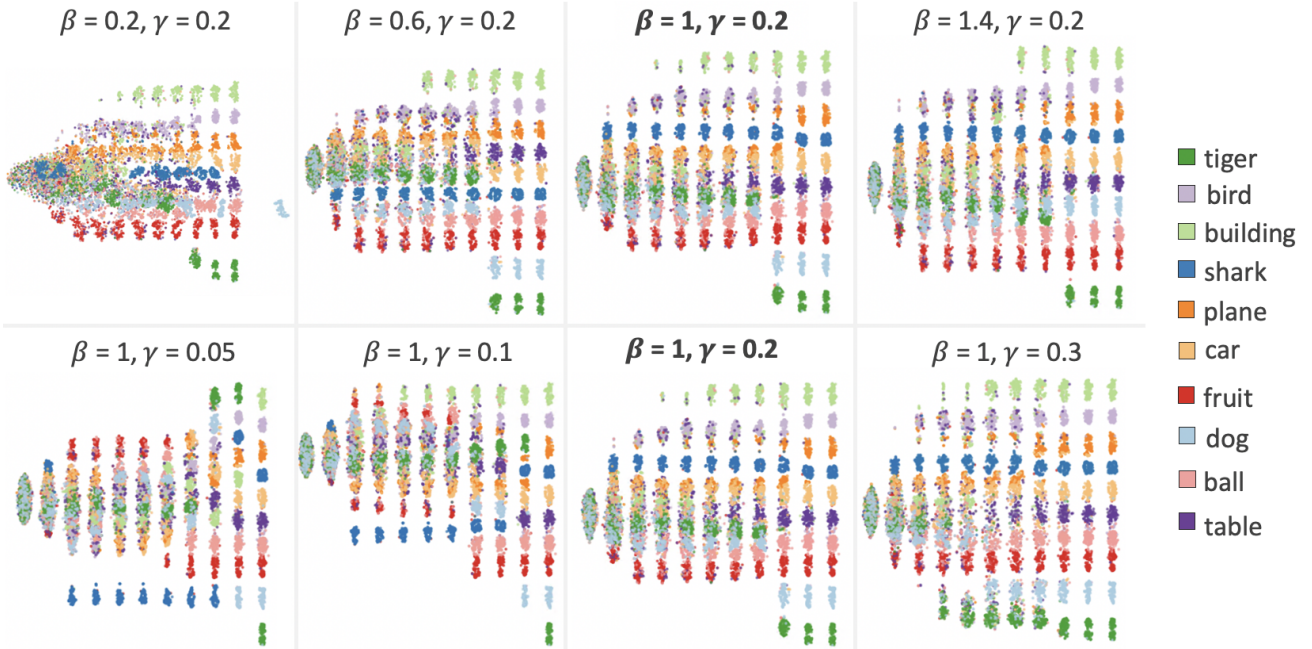


Fig. 11: **Exploring different β and γ weightings for the rectilinear layout losses C_d^c and C_a^c respectively, with $\alpha = 1$.** Similar to previous experiments, for $\beta \in \{1, 3\}$, the iterations exhibit poor separation, with unclear links between points and iteration steps. A minimum value of $\beta = 1$ is necessary to achieve sufficient separation and is hence selected. $\gamma = 0.05$ and $\gamma = 0.1$ result in inadequate alignment of clusters across iterations. While $\gamma = 0.2$ and $\gamma = 0.3$ produce satisfactory results, we choose $\gamma = 0.2$ to minimize disruptions to the t-SNE layout while allowing for alignment. The alignments are not smooth in some areas (see $\beta = 1, \gamma = 0.2$), such as the blue-green points between the 4th and 3rd lines from the right. Alignment is a tradeoff in these layouts, as limited movement makes optimization challenging. Increasing $\gamma = 0.3$ results in smoother alignments, but this comes at the expense of cluster quality, which is not desirable.

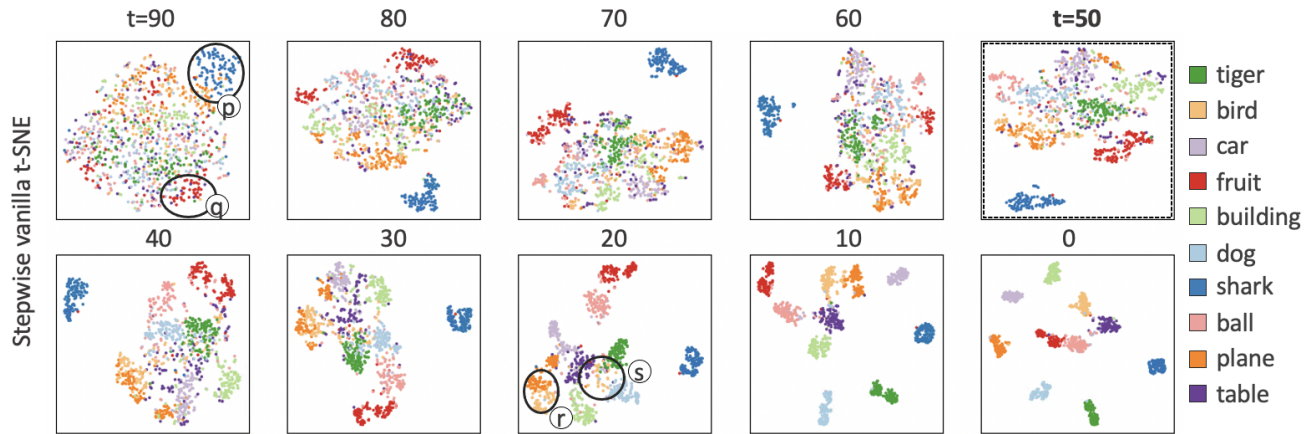


Fig. 12: **Visualizing the individual embeddings of the baseline stepwise vanilla t-SNE** for comparison with the proposed layouts. This shows the affect of C_s alone, i.e., $\alpha = 1, \beta = 0$, and $\gamma = 0$. Note that show embeddings from the second sampled time step (we skip $t = 100$). We observe that the overall cluster structures remain similar to the radial ($\alpha = 1, \beta = 1, \gamma = 0.05$), and rectilinear layouts ($\alpha = 1, \beta = 1, \gamma = 0.2$). For example, in all three the *dark blue* and *red* points of sharks and fruits emerge by the third line from the left or inner ring, i.e., $t = 80$. Also, the *dark* and *light orange* points of planes and birds are mixed until $t = 30$. This reflects the quality of our evolutionary embedding in maintaing clusters, while enabling the study of data progression more easily.



Fig. 13: **Our proof of concept front-end** enables analysis of the evolutionary embeddings produced by *EvolvED*. At the center (a) is our proposed evolutionary embedding, which is the outcome of *EvolvED*. The above shows the radial layout, but the rectilinear one can be retrieved with the buttons on the top-right of (a). Images corresponding to points at every n degree are displayed along the outer ring of the layout (a). A control panel on the left (b) supports data filtering, visualizing, and coloring options. Selected images are displayed on the right (c) in an image viewer to enable understanding of the embedding. Points can be filtered based on the iteration t , the path length (b.1), or prompt keywords (b.4). Some visualization options, such as deciding the number of images to be displayed on the outer ring, the smoothness of the paths, and the interpolation factor to group paths of a cluster, are provided (b.2). Points in the embedding can be encoded by adjustable colors based on the prompt or a keyword within a prompt (b.4). Lastly, images in the image viewer can be grouped by time step or color code to enable analysis (b.3).

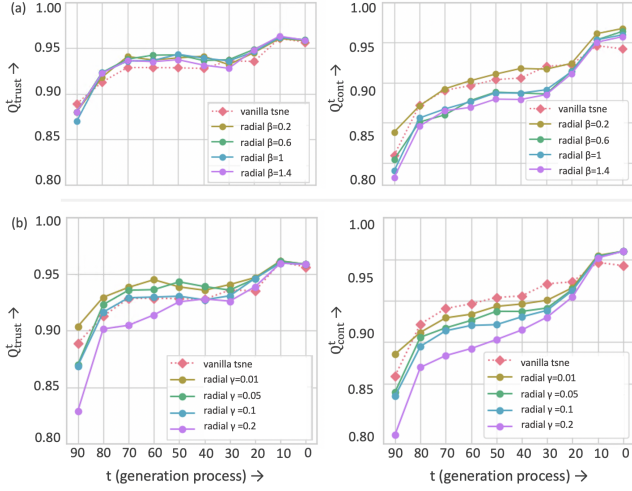


Fig. 14: Evaluating neighborhood preservation with Q^i_{trust} and Q^i_{cont} for the proposed radial layout across (a) different β values with $\alpha = 1$, $\gamma = 0.05$, and (b) different γ values with $\alpha = 1$, $\beta = 1$. Embeddings are derived from $\hat{\mathbf{h}}^i_{t-1}$. While Q^i_{trust} across various β values in (a) appear comparable, Q^i_{cont} exhibits noticeable variations. Despite $\beta = 0.2$ yielding the best Q^i_{cont} values, it resulted in poor visual separability between iterations shown in Fig. 10. Conversely, $\beta \in 0.6, 1$ are comparable in preserving high-dimensional neighborhoods. Hence, $\beta = 1$ was selected for improved iteration separation seen in Fig. 10. Further, Q^i_{cont} and Q^i_{trust} in (b) display degradation with $\gamma = 0.2$, while $\gamma \in 0.01, 0.05$ remain comparable in preserving neighborhoods. We hence choose $\gamma = 0.05$ since lower values result in insufficient alignment.

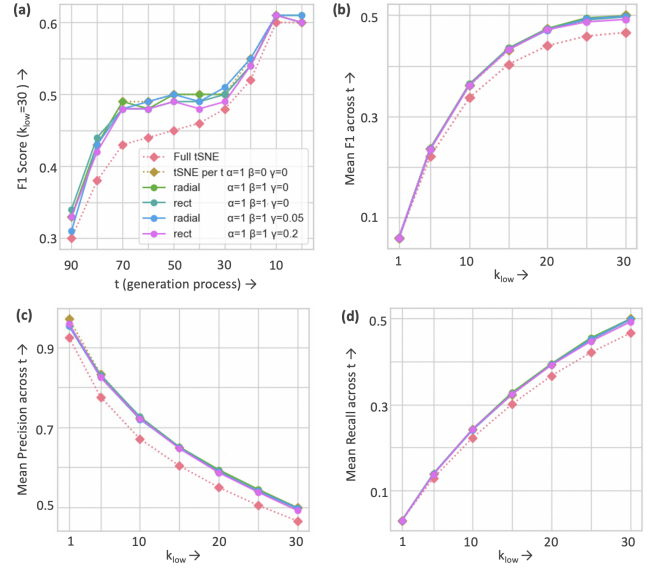


Fig. 16: Comparison of F1, Precision, and Recall for evolutionary embeddings vs. t-SNE baselines across low-dimensional neighbours k_{low} , t , and a fixed number of high-dimensional neighbours k_{high} . (a) F1 score progression across time steps for $k_{low} = 30$, comparing full vanilla t-SNE, stepwise vanilla t-SNE, and proposed radial and rectilinear layouts. (b-d) Average F1, Precision, and Recall across time steps for varying k_{low} . The radial and rectilinear layouts with different β and γ values, perform similarly to stepwise t-SNE in preserving semantic relations in the low-dimensional space, while full vanilla t-SNE consistently underperforms across all metrics.

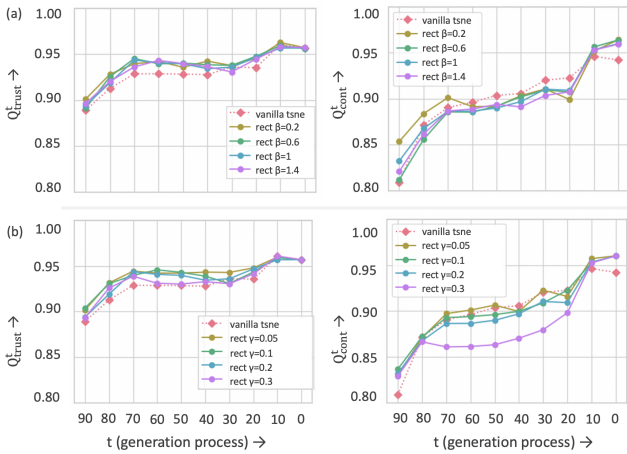


Fig. 15: Evaluating neighborhood preservation with Q^i_{trust} and Q^i_{cont} for the proposed rectilinear layout across (a) different β values with $\alpha = 1$, $\gamma = 0.2$, and (b) different γ values with $\alpha = 1$, $\beta = 1$. Embeddings are derived from $\hat{\mathbf{h}}^i_{t-1}$. Q^i_{trust} and Q^i_{cont} across various β (a) are comparable. However, in (b), Q^i_{cont} and Q^i_{trust} show degradation, especially when $\gamma = 0.3$. Lower γ values preserve neighborhoods similarly. In Fig. 11, both $\gamma = 0.2$ and $\gamma = 0.3$ led to good alignments; however, the neighborhood preservation deterioration with $\gamma = 0.3$ prompts our choice of $\gamma = 0.2$.

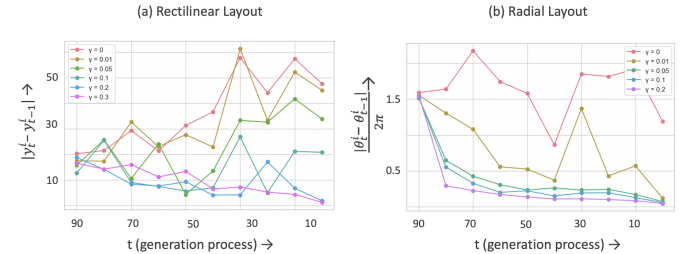


Fig. 17: Evaluation of the alignment constraint on vertical and angular displacements across rectilinear (a) and radial (b) layouts across γ values, with $\alpha = 1$ and $\beta = 1$. Without the alignment, there is erratic behavior in $\gamma = 0$. We also see such behavior when the γ values are small. We select $\gamma = 0.2$ for rectilinear and $\gamma = 0.05$ for radial as the first stable values that do not degrade clustering quality seen in Fig. 15 and 14 respectively. The rectilinear layout shows more jumps compared to the radial layout, likely due to the radial layout's added flexibility for point movement in two directions around the ring. In contrast, the rectilinear layout limits movement inward, making optimization more challenging. Additionally, for stable γ values ($\gamma < 0.2$ for rectilinear and $\gamma < 0.05$ for radial), alignment is poorer during the initial noisy steps (larger t) and gradually improves as generation progresses. This is likely due to the nature of the data itself, where initial steps generate more content with quickly changing clusters, while later steps focus on cluster refinement.

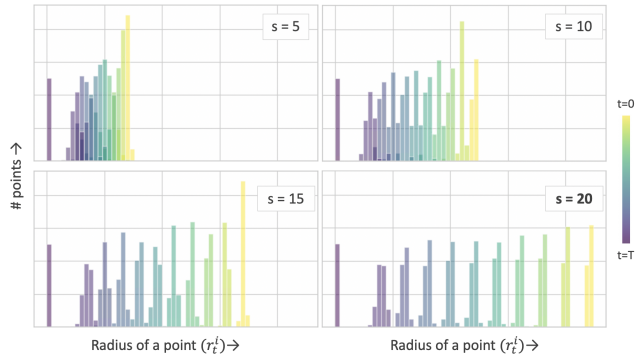


Fig. 18: **Exploring the hyperparameter spacing** s used to set the ring offsets (\bar{r}_i) per iteration, t , where $\bar{r}_i = (T - t) * s$. Here, histograms illustrate the distribution of polar radii r_i^t for radial embedding points I_i^t , projected from $\hat{\mathbf{h}}_i^t$ with $\alpha = 1$, $\beta = 1$, and $\gamma = 0.05$. Each histogram is color-coded by its corresponding iteration t , with T representing noise. A clear separation between iterations is observed when $s = 20$, prompting us to use this value for experiments. However, excessively large values of s run the risk of insufficient allocation of space for early time steps. We observe similar insights for the rectilinear layout at $s = 20$ hence we use the same value.

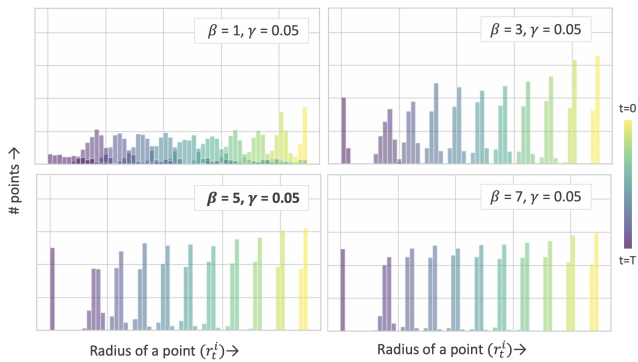


Fig. 19: **Exploring the iteration separation across β values** for the radial layout in a more systematic way. Histograms are used to illustrate the distribution of polar radii r_i^t for radial embedding points I_i^t , projected from $\hat{\mathbf{h}}_i^t$ with $\alpha = 1$, $\gamma = 0.05$, and $s = 20$. A clear separation between iterations is observed when $\beta = 1$. The same insights are used for the rectilinear layout at $\beta = 1$. We use the same value for both the radial and rectilinear layouts.